Supporting Information for

Compositionally Screened Eutectic Catalytic Coatings on Halide Perovskite Photocathode for Photo-Assisted Selective CO_2 Reduction

Jie Chen[†§+], *Jun Yin*[†+], *Xiaopeng Zheng*[†+], *Hassan Ait Ahsaine*[†§], *Yang Zhou*[†], *Chunwei Dong*[†], *Omar F. Mohammed*[†], *Kazuhiro Takanabe*[†§], *Osman M. Bakr*[†§*]

†King Abdullah University of Science and Technology (KAUST), Division of Physical Science and Engineering (PSE), §KAUST Catalysis Center (KCC), Thuwal 23955-6900, Saudi Arabia.

Corresponding author: osman.bakr@kaust.edu.sa (O. M. B.)

[+] These authors contributed equally.

Synthesis of the In-Bi-Sn metal alloys. Pure indium (99.99%), bismuth (99.99%) and tin (> 99%) granules and paraffin oil were purchased from Sigma-Aldrich. The procedure for synthesizing the metal alloys was inspired by studies on the synthesis of In-Sn,[1] Bi-Sn, Bi-In[2] alloy nanoparticles. As illustrated in Figure S1, certain molar ratios of In, Bi, and Sn metals were ground and mixed in a crucible to obtain mixed metal powders, which were then transferred to a vial containing 5 mL paraffin oil. In total, 21 samples were made with the feed molar ratios of the metals varied in 20% increments; all the ratios are summarized in Table S1. For example, to synthesize the $In_{0.6}Bi_{0.2}Sn_{0.2}$ sample, 0.6 mmol In, 0.2 mmol Bi and 0.2 mmol Sn were used. The mixed metal powders in the vial were melted to alloy spheres under continuous stirring (500 rpm) and heating (300 ℃) on a hot plate. After 2 hours, the vial was cooled to room temperature, and metal alloy spheres were formed. In this process, the paraffin oil acted as a solvent for dispersing the metal powders and as a protective agent to avoid the oxidation of the metals under high temperature. The as-obtained metal alloy spheres were cleaned with ethanol and acetone to remove the paraffin oil from their surface. Then, the spheres were re-melted between two glass slides on the hot plate at 150-200 ℃. Pressure exerted by a 1-kg bottle was applied on the upper glass slide to press the alloy spheres into a thin-film electrode. The thickness of the thin-film electrodes was approximately 500 μm.

Perovskite solar cell fabrication. A one-step-processed methylammonium lead iodide ($MAPbI_3$)-based solar cell was fabricated by the antisolvent extraction approach in a N_2 glove box. The hole transport layer (HTL) poly(bis(4-phenyl)(2,4,6-trimethylphenyl)amine) (PTAA), with a concentration of 2 mg/ml in toluene, was spin-coated at 6,000 rpm for 35 s and then annealed at 100 °C for 10 min. The $MAPbI_3$ perovskite precursor solution was prepared by dissolving 460 mg PbI_2 and 159 mg MAI in 700 μL DMF and 78 μL DMSO. Then, 100 μL of the precursor solution was spun onto PTAA at 4000 rpm for 30 s; the sample was quickly washed with 200 μL toluene. Subsequently, the sample was annealed at 65 °C for 10 min and 100 °C for 10 min. Device construction was completed by thermally evaporating C_{60} (20 nm), 2,9-dimethyl-4,7-diphenyl-1,10-phenanthroline (BCP, 8 nm) and copper (80 nm) successively.

Metal alloy/Perovskite photocathode fabrication. Notably, electrons generated in the perovskite photovoltaic will flow out from the C_{60}/BCP/Cu electron transporting layer for possible reductive reactions. A piece of catalytic metal alloy was thus melted and quickly spread onto the C_{60}/BCP/Cu layer of the perovskite photovoltaic. The exposed area of the catalytic alloy was 0.5 cm^2. As In-Bi-Sn alloys generally have a low melting point (~ 100 °C), quick contact with the hot melted alloys will not damage the perovskite materials. The exposed FTO area of the perovskite photovoltaic was connected to a piece copper tape, whose other end was connected to a potentiostat.

Characterization of the perovskite photovoltaic. Simulated AM 1.5G irradiation (100 mW/cm^2) was produced by a Newport Sol3A solar simulator with a 450-W xenon source and a 2 × 2 inch illuminated area for current-voltage measurements. The light intensity was calibrated by the reference cell and meter, which consisted of a readout device and a 2 × 2 cm calibrated solar cell made of monocrystalline silicon. The photocurrent was recorded by a Keithley Model 2400 Source-Meter at a scanning rate of 0.1 V s^{-1}.

Characterization of the metal alloys. Scanning electron microscopy (SEM) and X-ray energy dispersive spectroscopy (EDS) were conducted using a Zeiss Merlin SEM. X-ray diffraction (XRD) patterns were recorded on a Bruker D8 Advance A25 diffractometer equipped with a Cu X-ray tube (Cu–Kα; λ = 0.154 nm) operated at 40 kV and 40 mA. The resistivities of the samples were measured using a four-point probe station form Advanced Instrument Technology, Model CMT-SR2000N. The resistivities of $In_{0.4}Bi_{0.6}$, $In_{0.4}Sn_{0.6}$, $Bi_{0.4}Sn_{0.6}$, and $In_{0.6}Bi_{0.2}Sn_{0.2}$ are 0.662 mΩ·cm, 0.112 mΩ·cm, 0.149 mΩ·cm and 0.511 mΩ·cm, respectively. The thickness of the coating layer was measured using a digimatic caliper roller from Mitutoyo Corp., Model No. CD-6" ASX.

Electrochemical measurements. Electrochemical measurements were conducted using a homemade electrochemical cell and a BioLogic© VMP3 potentiostat. A typical three-electrode structure was employed with a Pt wire and a Ag/AgCl electrode (in saturated KCl) used as the counter electrode and reference electrode, respectively. The counter electrode was isolated with a ceramic frit to suppress product crossover. As an electrolyte, 0.1 M $KHCO_3$ (99.99%, metal basis, Sigma-Aldrich) was used. Prior to the measurements, the electrolyte was purged with Ar for 0.5 h to evacuate O_2 from the electrolyte and then

saturated with CO_2 for 0.5 h. A continuous purge of CO_2 was maintained during the electrolysis, providing large current densities for the CO_2 reduction products to minimize the mass-transport limitations. A flow rate of 20 sccm was used to ensure sufficient CO_2 transport to the electrode surface while preventing interference from gas bubbles striking the electrode. All of the applied potentials were recorded against a Ag/AgCl (saturated KCl) reference electrode and then converted to values relative to a reversible hydrogen electrode (RHE) using the equation E (vs. RHE) = E (vs. Ag/AgCl) + 0.197 V + 0.0591 V × pH.

Product identification. An offline high-performance liquid chromatograph (HPLC, Agilent 1200 series) and an online micro gas chromatograph (SRI instruments, T-3000) were employed to confirm the identities and quantities of the liquid- and gas-phase products during the electrochemical reactions, respectively. A packed MolSieve 5A equipped with a thermal conductivity detector (TCD) was used for analysis of the gaseous products. The HPLC was equipped with an ICE-Coregel 87 H3 column to quantify the liquid products. The minimum detection limit for gaseous products was 50 ppm.

Photoelectrochemical measurements. Simulated AM 1.5G irradiation (100 mW/cm^2) was produced by a XES-40S2-CE solar simulator with a 2 × 2 inch illuminated area. The light intensity was calibrated by the reference cell and meter, which consisted of a readout device and a 2 × 2 cm calibrated solar cell made of monocrystalline silicon. The electrochemical measurements and product identification were kept the same as the electrocatalysis measurements for the individual metal electrode.

Calculation of the photo-assisted electrocatalysis efficiency. The photo-assisted electrolysis system efficiency, η_{PAE}, was calculated by equation 1:

$$\eta_{PAE} = \frac{P_{f,o}}{P_s + P_{e,i}} \quad \text{(eq. 1)}$$

where $P_{f,o}$ is the output power density contained in the chemical fuel produced, P_s is the incident illumination power density (100 mW/cm^2), and $P_{e,i}$ is the input electrical power density. In our system, the energy was stored mostly in HCOOH with a FE of 99%. Therefore, $P_{f.o}$ was calculated by equation 2:

$$P_{f,o} = J_{op} \times FE_{HCOOH} \times E_{HCOOH} \quad \text{(eq. 2)}$$

where J_{op} is the overall current density (~5.5 mA/cm^2), FE_{HCOOH} is the faradaic efficiency and E_{HCOOH} is the potential difference corresponding to the Gibbs free-energy difference between the two half-reactions for the HCOOH produced at the cathode and for water oxidation at the anode, which is 1.48 V according to the literature.[3] $P_{e,i}$ was then calculated by equation 3:

$$P_{e,i} = J_{op} \times E_{e,i} \quad \text{(eq. 3)}$$

where $E_{e,i}$ is the total bias applied to the system, which is the voltage required in a two-electrode electrolysis measurement. In the current system using a perovskite photocathode and Pt wire as an anode, at 0.6 V vs. RHE, $V_{e,i}$ was determined to be 2.23 V by recording the E_{ce} value using the EC-Lab software. Using the abovementioned values and equations, the η_{PAE} was determined to be 7.2%.

Computational Details. Density functional theory (DFT) calculations were performed using the Vienna Ab initio Simulation Package (VASP).[4-5] The projector augmented wave (PAW) approach together with the Perdew-Burke-Ernzerhof (PBE) formulation of the generalized gradient functional (GGA) for exchange-correlation energy was used. The energy cutoff for the wave function expanded in the plane-wave basis was 500 eV. Slabs with 8 atomic layers expose the (100) surface for In and Sn, and the slabs expose the (001) surface for Bi, In_2Bi, In_5Bi_3, and InBi. All slabs were separated by a vacuum layer (~15 Å) to prevent spurious inter-slab interactions. The Monkhorst−Pack-type *k*-mesh was set to 4×4×4 for bulk In, Bi, Sn, In_2Bi, In_5Bi_3, and InBi and to 4×4×1 for their corresponding slabs. For CO_2 reduction, starting from the adsorption of bicarbonate (CO_3H*), the two intermediates COOH* and HCOO* were considered for CO and HCOO- production. For H_2O reduction, starting from the absorption of H_2O molecules on the alloy surfaces, H* was considered for H_2 production. Each crystal structure was optimized until the forces on every single atom were smaller than 0.02 eV/Å. The molecular graphics viewer VESTA was used to plot crystal structures.

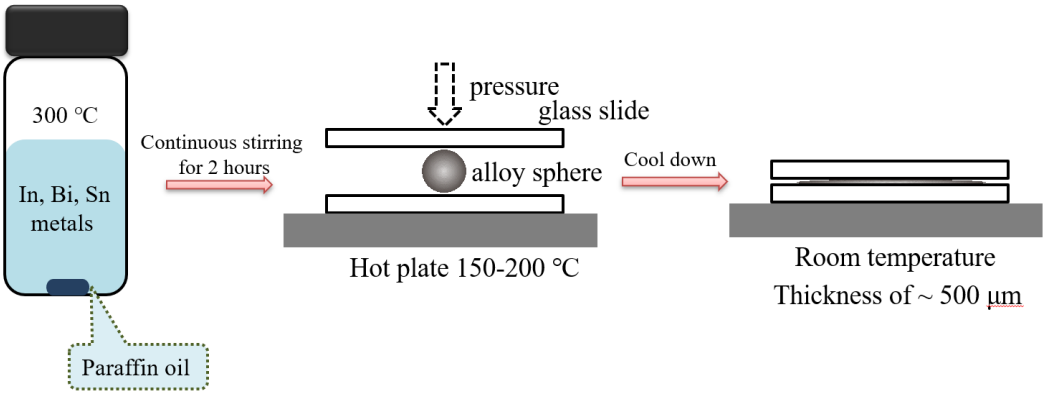

Figure S1. Illustration of the mechanical alloying process of the In-Bi-Sn alloys in paraffin oil.

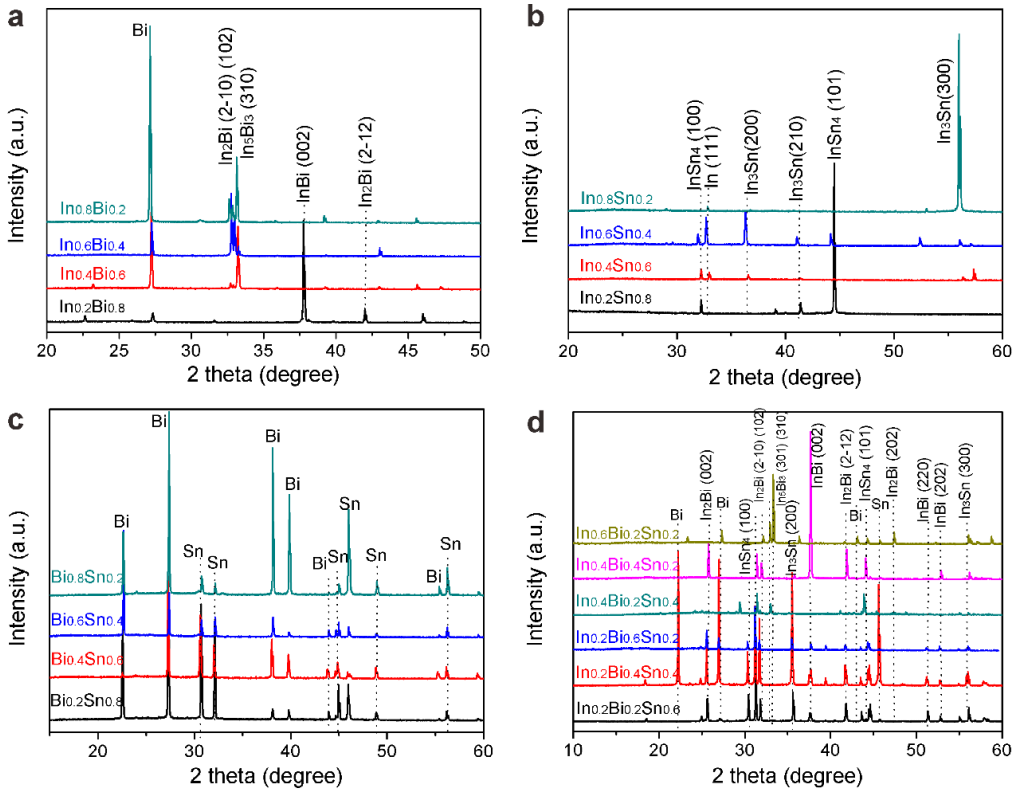

Figure S2. XRD patterns for (a) In-Bi, (b) In-Sn, (c) Bi-Sn and (d) In-Bi-Sn alloys with varying feed molar ratios. The crystals phases are summarized in Table S1.

As shown in Figure S3, several redox peaks can be found in the cyclic voltammograms of the metal alloy electrodes. These peaks correspond to the reduction of the metal oxide species on the surface of the electrodes. In the case of In-Bi alloy (Figure S3a), the peak at ~0 V vs. RHE is associated with the reduction of Bi_2O_3,[6] whereas the peak at ~-0.45 V vs. RHE is associated with the reduction of In_2O_3.[7] In the case of In-Sn alloy (Figure S3b), the peak at

~-0.4 V vs. RHE is due to the overlapping of the reduction peaks of In_2O_3 and SnO_x. In the case of Bi-Sn alloy (Figure S3c), the peak at ~-0.3 V vs. RHE is associated with the reduction of SnO_x.[8] In the case of the In-Bi-Sn ternary alloy (Figure S3d), the small peak at ~ 0 V vs. RHE is associated with the reduction of Bi_2O_3, while the peak at ~-0.4 V vs. is due to the overlapping of the reduction peaks of In_2O_3 and SnO_x.

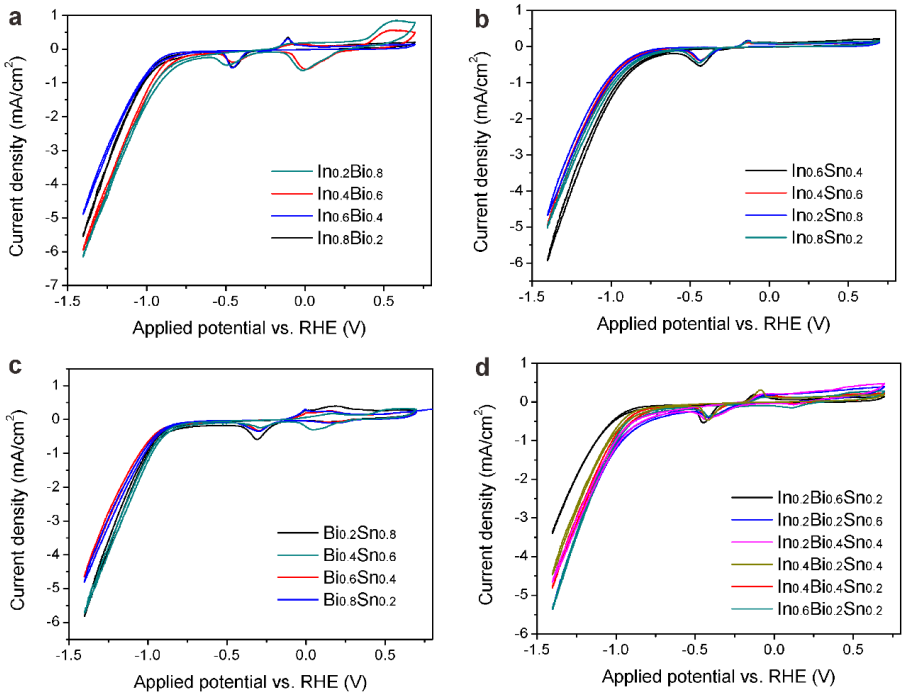

Figure S3. Cyclic voltammograms of the (a) In-Bi alloy, (b) In-Sn alloy, (c) Bi-Sn alloy, (d) In-Bi-Sn alloy electrodes in 0.1 M $KHCO_3$ solution. The scan rate was 50 mV/s. From these CV curves, we derived the onset potential for

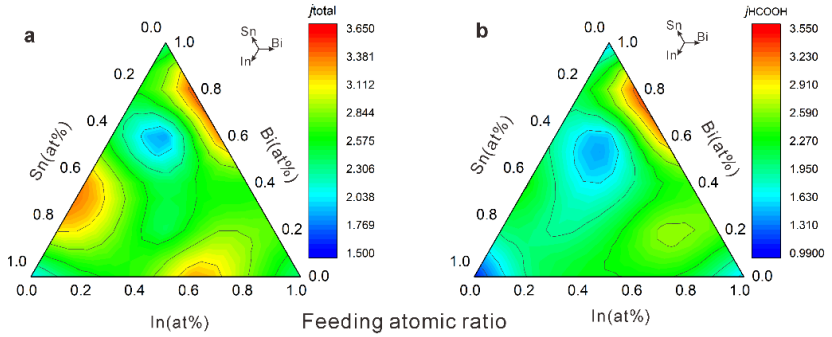

Figure S4. The ternary contour figure for the (a) total current density and the (b) partial current density for the electrodes of In-Bi-Sn alloys. The figure was drawn by using the feed atomic ratio of the alloy electrodes.

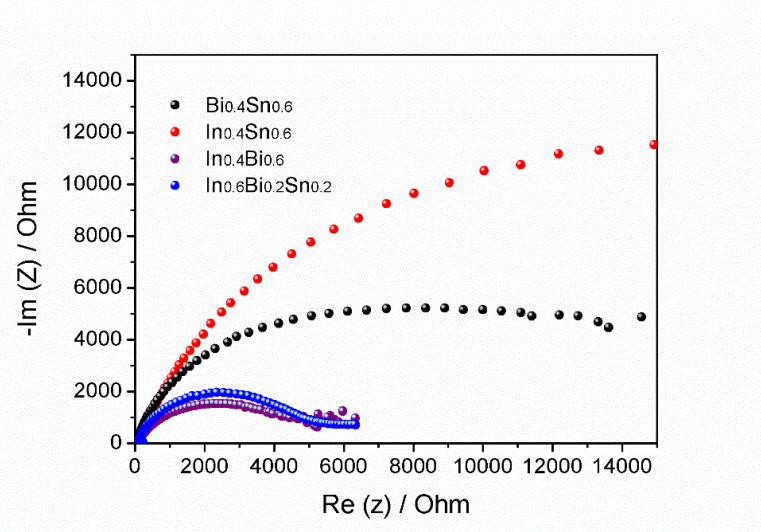

Figure S5. Nyquist plots for the electrochemical impedance spectroscopy (EIS) analysis of the representative $In_{0.4}Bi_{0.6}$, $In_{0.4}Sn_{0.6}$, $Bi_{0.4}Sn_{0.6}$, $In_{0.6}Bi_{0.2}Sn_{0.2}$ samples in CO_2-saturated 0.1 M $KHCO_3$ solution.

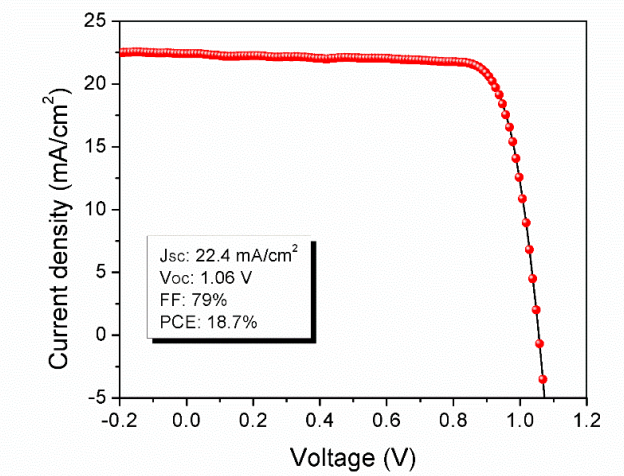

Figure S6. The current density vs. voltage curve of the halide perovskite solar cell made by using $MAPbI_3$ as the active-layer material.

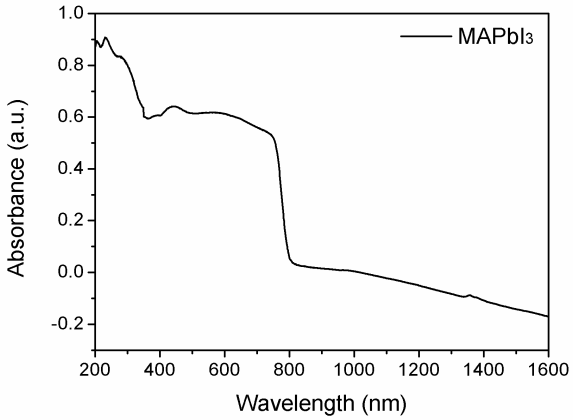

Figure S7. Light absorption spectra of the $MAPbI_3$ material.

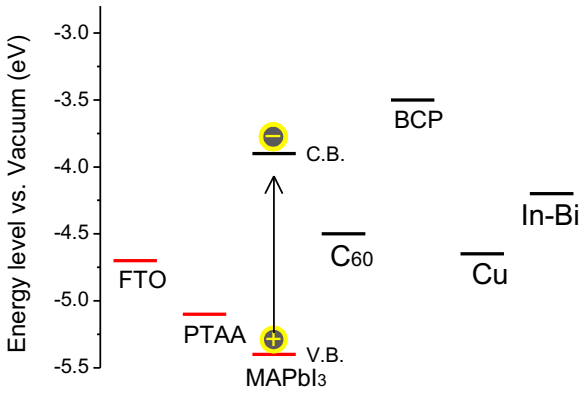

Figure S8. Energy levels (vs. Vacuum) of the components in the photoelectrode.

Table S1. The feed atomic ratio, actual surface atomic ratio, crystal phases, onset potential and faradaic efficiency for HCOOH formation over the In-Bi-Sn alloys. [a]Note: the onset potentials were taken at partial current density of 0.5 mA/cm^2 for HCOOH production.

Feed atomic ratio			Actual surface atomic ratio			Crystal phases	Onset potential (at 0.5 mA/cm^2)[a] V vs. RHE	FE (HCOOH)
In	Bi	Sn	In	Bi	Sn			
0	0	1	0	0	1	Sn	/	50
0	0.2	0.8	0	0.15	0.85	Bi+Sn	-0.97	64
0	0.4	0.6	0	0.29	0.71	Bi+Sn	-0.94	70
0	0.6	0.4	0	0.32	0.68	Bi+Sn	-0.98	78
0	0.8	0.2	0	0.46	0.54	Bi+Sn	-0.96	83
0	1	0	0	1	0	Bi	/	60
0.2	0	0.8	0.48	0	0.52	$InSn_4$, In_3Sn	-0.93	81

0.2	0.2	0.6	0.34	0.33	0.33	In_2Bi, $InSn_4$, In_3Sn, InBi, In_2Bi, In_3Sn	-0.91	63
0.2	0.4	0.4	0.29	0.36	0.35	Bi, In_2Bi, $InSn_4$, In_3Sn, InBi, Sn In_2Bi, In_3Sn	-0.94	60
0.2	0.6	0.2	0.27	0.33	0.4	Bi, In_2Bi, $InSn_4$, In_3Sn, InBi, Sn In_2Bi, In_3Sn	-0.93	81
0.2	0.8	0	0.48	0.52	0	Bi, InBi, In_2Bi	-0.82	97
0.4	0	0.6	0.62	0	0.38	$InSn_4$, In, In_3Sn	-0.93	85
0.4	0.2	0.4	0.48	0.25	0.27	Bi, In_2Bi, $InSn_4$, In_3Sn, InBi, Sn In_2Bi, In_3Sn, In_5Bi_3	-0.94	95
0.4	0.4	0.2	0.43	0.33	0.24	Bi, In_2Bi, $InSn_4$, In_3Sn, InBi, Sn In_2Bi, In_3Sn	-0.94	75
0.4	0.6	0	0.46	0.54	0	Bi, In_5Bi_3	-0.83	98
0.6	0	0.4	0.71	0	0.29	$InSn_4$, In, In_3Sn	-0.89	66
0.6	0.2	0.2	0.67	0.24	0.09	Bi, In_2Bi, $InSn_4$, In_3Sn, InBi, Sn In_2Bi, In_3Sn, In_5Bi_3	-0.89	95
0.6	0.4	0	0.67	0.33	0	Bi, In_2Bi, In_5Bi_3	-0.96	90
0.8	0	0.2	0.9	0	0.1	$InSn_4$, In, In_3Sn	-0.90	78
0.8	0.2	0	0.78	0.22	0	Bi, In_2Bi, In_5Bi_3	-0.94	91
1	0	0	1	0	0	In	/	65

Table S2. Comparison of the performance of CO_2 electroreduction to HCOOH over the as-reported electrocatalysts.

Metal/Alloys	Electrolyte	Primary Product	Second Product	Faradic Efficiency	Selectivity	Current density (mA/cm^2)	Potential (V vs. RHE)	Overpotential	Ref
$In_{0.4}Bi_{0.6}$	0.1 M $KHCO_3$	HCOOH	H_2	98%	~98%	~3.5	-1.2		This work
$In_{0.2}Bi_{0.8}$	0.1 M $KHCO_3$	HCOOH	H_2	97%	97%	~3.7	-1.2		
$In_{0.6}Bi_{0.2}Sn_{0.2}$	0.1 M $KHCO_3$	HCOOH	H_2	95%	94%	~3.1	-1.2		
Bulk In	0.1 M $KHCO_3$	HCOOH	H_2	94.9%	94.6%	5	-1.55	/	[9]
Bulk Sn	0.1 M $KHCO_3$	HCOOH	CO	88.4%	88.3%	5	-1.48	/	[9]
Sn quantum sheets in Graphene	0.1 M $NaHCO_3$	HCOOH	H_2	89%	~90%	21.1	-1.16	/	[10]
SnO_2 NPs on graphene	0.1 M $NaHCO_3$	HCOOH	H_2	93%	~93%	on carbon black (6.2); on graphene (13.1)	-1.16	~340 mV	[11]
Atomic Co layers	0.1 M Na_2SO_4	HCOOH	H_2	90.1%	90%	10.59	~-0.21	~240 mV	[12]
Pd_xPt/C	0.1 M KH_2PO_4/0.1 M K_2HPO_4	HCOOH	H_2	88%	/	5	-0.4	/	[13]
Sn-pNWs	0.1 M $KHCO_3$	HCOOH	CO	80%	/	~5	-0.8	350 mV	[14]
Cu_5Zn_8	0.1 M $KHCO_3$	HCOOH	CO	71.11%	/	~1	~-0.4	/	[15]
$Bi_2O_2CO_3$ Nanosheets	0.1 M $KHCO_3$	HCOOH	/	83%	/	~1	~-0.6	590 mV	[16]
Ultrathin Bi	0.5 M $NaHCO_3$	HCOOH	H_2	>95%	/	11	~-0.86	400 mV	[17]

Table S3. Comparison of the performance of CO_2 electroreduction to HCOOH over the as-reported photocathodes; [a] without external bias.

Photocathodes	Anodes	Conditions	Faradaic efficiency	Selectivity	Current density	Energy conversion efficiency	Ref
$In_{0.4}Bi_{0.6}$/perovskite	Pt wire	0.1 M $KHCO_3$ AM 1.5 G -0.6 V vs. RHE	99%	~98%	5.5 mA/cm^2	7.2%	This work
SnO_2 NWs/silicon	Pt gauze	0.1 M $KHCO_3$ AM 1.5 G -0.4 V vs. RHE	60%	60%	10 mA/cm^2	11%	3
Cu-decorated Co_3O_4 nanotube arrays	Pt foil	0.1 M Na_2SO_4 Visible light -0.9 V vs. SCE	/	~100%	/	/	18
Polycrystalline Mg-doped $CuFeO_2$	Pt mesh	0.1 M $NaHCO_3$ LED source -0.9 V vs. SCE	10%	/	/	/	19
$CuFeO_2$/CuO	Pt foil	0.1 M $KHCO_3$ AM 1.5 G	>90%	90%	/	1%[a]	20
[Ru(L-L)$(CO)_2$]n polymer modified Zn-doped p-InP	glassy carbon	Water Visible light -0.6 V vs. Ag/AgCl	62%	/	/	/	21
RuCE+RuCA modified $Cu_2ZnSn(S,Se)_4$	glassy carbon	Water Visible light -0.6 V vs. Ag/AgCl	80%	/	/	/	22
Pyridine/P-CdTe	Pt wire	0.1 M $NaHCO_3$ Visible light -0.6 V vs. SCE	60.7%	/	4.19 mA/cm^2	/	23
P-InP/Ru complex	Pt loaded TiO_2	0.1 M $NaHCO_3$ AM 1.5 G	>70%	/	/	0.03-0.04%[a]	24

References in the Supporting Information:

1. Zhao, Y.; Zhang, Z.; Dang, H. Synthesis of In–Sn Alloy Nanoparticles by a Solution Dispersion Method. *J. Mater. Chem.* **2004,** *14* (3), 299-302.

2. V. B. Kumar; G. Kimmel; Z. Porat; Gedanken, A. Formation of Particles of Bismuth-Based Binary Alloys and Intermetallic Compounds by Ultrasonic Cavitation. *New J. Chem.* **2015,** *39*, 5374-5381.

3. Zhang, N.; Long, R.; Gao, C.; Xiong, Y. Recent Progress on Advanced Design for Photoelectrochemical Reduction of CO_2 to Fuels. *Sci. China Mater.* **2018,** *61* (6), 771-805.

4. Kresse, G.; Hafner, J. Ab Initio Molecular Dynamics for Open-Shell Transition Metals. *Phys. Rev. B* **1993,** *48* (17), 13115-13118.

5. Kresse, G.; Furthmuller, J. Efficient Iterative Schemes For Ab Initio Total-Energy Calculations Using a Plane-Wave Basis Set. *Phys. Rev. B* **1996,** *54* (16), 11169-11186.

6. Frena, M.; Campestrini, I.; de Braga, O. C.; Spinelli, A. In Situ Bismuth-Film Electrode for Square-Wave Anodic Stripping Voltammetric Determination of Tin in Biodiesel. *Electrochim. Acta* **2011,** *56* (12), 4678-4684.

7. White, J. L.; Bocarsly, A. B. Enhanced Carbon Dioxide Reduction Activity on Indium-Based Nanoparticles. *J. Electrochem. Soc.* **2016,** *163* (6), H410-H416.

8. Baruch, M. F.; Pander, J. E.; White, J. L.; Bocarsly, A. B. Mechanistic Insights into the Reduction of CO_2 on Tin Electrodes Using In Situ ATR-IR Spectroscopy. *ACS Catal.* **2015,** *5* (5), 3148-3156.

9. Y. Hori; H. Wakebe; T. Tsukamoto; Koga, O. Electrocatalytic Process of CO Selectivity in Electrochemical Reduction of CO_2 at Metal Electrodes in Aqueous Media. *Electrochim. Acta* **1994,** *39* (11-12), 1833-1839.

10. Lei, F.; Liu, W.; Sun, Y.; Xu, J.; Liu, K.; Liang, L.; Yao, T.; Pan, B.; Wei, S.; Xie, Y. Metallic Tin Quantum Sheets Confined in Graphene Toward High-Efficiency Carbon Dioxide Electroreduction. *Nat. Commun.* **2016,** *7*, 12697.

11. Zhang, S.; Kang, P.; Meyer, T. J. Nanostructured Tin Catalysts for Selective Electrochemical Reduction of Carbon Dioxide to Formate. *J. Am. Chem. Soc.* **2014,** *136* (5), 1734-1737.

12. Gao, S.; Lin, Y.; Jiao, X.; Sun, Y.; Luo, Q.; Zhang, W.; Li, D.; Yang, J.; Xie, Y. Partially Oxidized Atomic Cobalt Layers for Carbon Dioxide Electroreduction to Liquid Fuel. *Nature* **2016,** *529* (7584), 68-71.

13. Kortlever, R.; Peters, I.; Koper, S.; Koper, M. T. M. Electrochemical CO_2 Reduction to Formic Acid at Low Overpotential and with High Faradaic Efficiency on Carbon-Supported Bimetallic Pd–Pt Nanoparticles. *ACS Catal.* **2015,** *5* (7), 3916-3923.

14. B. Kumar; V. Atla; J. P. Brian; S, K.; T. Q. Nguyen; M, S.; Spurgeon, J. M. Reduced SnO_2 Porous Nanowires with a High Density of Grain Boundaries as Catalysts for Efficient Electrochemical CO_2-into-HCOOH Conversion. *Angew. Chem. Int. Ed.* **2017,** *56*, 3645-3649.

15. G. Yin; H. Abe; R. Kodiyath; S. Ueda; N. Srinivasan; A. Yamaguchi; Miyauchi, M. Selective Electro- or Photo-reduction of Carbon Dioxide to Formic Acid using a Cu-Zn Aloy Catalyst. *J. Mater. Chem. A* **2017,** *5*, 12113-12119

16. Lv, W.; Bei, J.; Zhang, R.; Wang, W.; Kong, F.; Wang, L.; Wang, W. $Bi_2O_2CO_3$ Nanosheets as Electrocatalysts for Selective Reduction of CO_2 to Formate at Low Overpotential. *ACS Omega* **2017,** *2* (6), 2561-2567.

17. Han, N.; Wang, Y.; Yang, H.; Deng, J.; Wu, J.; Li, Y. Ultrathin Bismuth Nanosheets From In Situ Topotactic Transformation for Selective Electrocatalytic CO_2 Reduction to Formate. *Nat. Commun.* **2018,** *9* (1), 1320.

18. Shen, Q.; Chen, Z.; Huang, X.; Liu, M.; Zhao, G. High-Yield And Selective Photoelectrocatalytic Reduction of CO_2 to Formate by Metallic Copper Decorated Co_3O_4 Nanotube Arrays. *Environ. Sci. Technol.* **2015,** *49* (9), 5828-35.

19. Gu, J.; Wuttig, A.; Krizan, J. W.; Hu, Y.; Detweiler, Z. M.; Cava, R. J.; Bocarsly, A. B. Mg-Doped $CuFeO_2$ Photocathodes for Photoelectrochemical Reduction of Carbon Dioxide. *J. Phys. Chem. C* **2013,** *117* (24), 12415-12422.

20. Unseock Kang; Sung Kyu Choi; Dong Jin Ham; Sang Min Ji; Wonyong Choi; Dong Suk Han; Abdel-Wahab, A.; Park, H. Photosynthesis of Formate From CO_2 and Water at 1% Energy Efficiency via Copper Iron Oxide Catalysis. *Energy Environ. Sci.* **2015,** *8*, 2638-2643

21. Arai, T.; Sato, S.; Uemura, K.; Morikawa, T.; Kajino, T.; Motohiro, T. Photoelectrochemical Reduction of CO_2 in Water Under Visible-Light Irradiation by a P-Type InP Photocathode Modified with an Electropolymerized Ruthenium Complex. *Chem. Commun.* **2010,** *46* (37), 6944-6.

22. Takeo Arai; Shin Tajima; Shunsuke Sato; Keiko Uemura; Takeshi Morikawa; Kajino, T. Selective CO_2 Conversion to Formate in Water Using a CZTS Photocathode Modified with a Ruthenium Complex Polymer. *Chem. Commun.* **2011,** *47*, 12664-12666.

23. Jeon, J. H.; Mareeswaran, P. M.; Choi, C. H.; Woo, S. I. Synergism Between CdTe Semiconductor and Pyridine – Photoenhanced Electrocatalysis for CO_2 Reduction to Formic Acid. *RSC Adv.* **2014,** *4* (6), 3016-3019.

24. Sato, S.; Arai, T.; Morikawa, T.; Uemura, K.; Suzuki, T. M.; Tanaka, H.; Kajino, T. Selective CO_2 Conversion to Formate Conjugated with H_2O Oxidation Utilizing Semiconductor/Complex Hybrid Photocatalysts. *J. Am. Chem. Soc.* **2011,** *133* (39), 15240-15243.